

In Search of The Optimal Atmospheric River Index for US Precipitation: A Multifactorial Analysis

Chen Zhang¹, Wen-wen Tung^{1*}, William S. Cleveland^{2,3}

¹Department of Earth, Atmospheric, and Planetary Sciences, Purdue University, West Lafayette, IN, USA

²Department of Statistics, Purdue University, West Lafayette, IN, USA

³Department of Computer Science, Purdue University, West Lafayette, IN, USA

Key Points:

- We consider an optimal AR index based on the precipitation effects that depend on regional physical mechanisms, seasons, and AR duration.
- *IWV* with 75th percentile climate threshold can capture the broad presence and accumulation of precipitation in both regions studied.
- Changing climatological threshold for detecting Midwest ARs results in a seasonal shift of maximum event-accumulated precipitation.

*Department of Earth, Atmospheric, and Planetary Sciences, Purdue University, 550 Stadium Mall Drive,
West Lafayette, IN 47907, USA

Corresponding author: Wen-wen Tung, wwtung@purdue.edu

Abstract

Atmospheric rivers (ARs) affect surface hydrometeorology in the US West Coast and Midwest. We systematically sought optimal AR indices for expressing surface precipitation impacts within the Atmospheric River Tracking Method Intercomparison Project (ARTMIP) framework. We adopted a multifactorial approach. Four factors—moisture fields, climatological thresholds, shape criteria, and temporal thresholds—collectively generated 81 West Coast AR indices and 81 Midwest indices from January 1980 to June 2017. Two moisture fields were extracted from the MERRA-2 data for ARTMIP: integrated water vapor transport (*IVT*) and integrated water vapor (*IWV*). CPC US Unified Precipitation data were used. Metrics for precipitation effects included two-way summary statistics relating the concurrence of AR and that of precipitation, per-event averaged precipitation rate, and per-event precipitation accumulation. We found that an optimal AR index for precipitation depends on the types of impact to be addressed, associated physical mechanisms in the affected regions, timing, and duration. In West Coast and Midwest, *IWV*-based AR indices identified the most abundant AR event time steps, most accurately associated AR to days with precipitation, and represented the presence of precipitation the best. With a lower climatological threshold, they detected the most accumulated precipitation with the longest event duration. Longer duration thresholds also led to higher accumulated precipitation, holding other factors constant. *IWV*-based indices are the overall choice for Midwest ARs under varying seasonal precipitation drivers. *IVT*-based indices suitably capture the accumulation of intense orographic precipitation on the West Coast. Indices combining *IVT* and *IWV* identify the fewest, shortest, but most intense AR precipitation episodes.

Plain Language Summary

[Atmospheric rivers (AR), the long narrow filaments of enhanced water vapor transport in the lower troposphere, are known to accompany extreme rain and winds. They are important weather systems for US water resources on the West Coast and in the Midwest. In our study, we asked which impacts, in which region, and in what time scale and period were of concern. We then used an approach combining climate significant- or extreme-event criteria, image processing, and statistical analysis to create 81 West Coast AR indices and 81 Midwest indices from January 1980 to June 2017 for answering the questions with detailed visualization. We found that an optimal AR index for precipitation

46 depends on the defined precipitation impacts, regional physical mechanisms of precip-
47 itation, season, and duration. Integrated water vapor (*IWV*) can represent the broad-
48 stroke presence and accumulation of precipitation in regions studied. Longer duration
49 thresholds also led to higher accumulated precipitation. Combined moisture with wind
50 fields using integrated water vapor transport (*IVT*), is necessary to get extreme West
51 Coast AR orographic precipitation. *IWV* well represents moderate to extreme Midwest
52 AR precipitation events for all seasons. Combination of *IVT* and *IWV* is useful to get
53 snapshots of extreme precipitation events.]

54 1 Introduction

55 Atmospheric rivers (ARs) are long, narrow filaments of enhanced water vapor trans-
56 port that is typically associated with a low-level jet and extratropical cyclone (Ralph et
57 al., 2018). When these moisture-laden ARs make landfall or penetrate inland, water va-
58 por condenses and can release enhanced precipitation (e.g., Guan et al., 2010, 2013; Luo
59 & Tung, 2015). AR precipitation in many parts of the world is paramount for water re-
60 sources (e.g., Guan et al., 2010; Dettinger et al., 2011; Rutz & Steenburgh, 2012; Det-
61 tinger, 2013; Lavers & Villarini, 2015; Eiras-Barca et al., 2016; Blamey et al., 2018; Lit-
62 tle et al., 2019). However, heavy rainfall can lead to floods and ensuing socioeconomic
63 damage. Studies have shown that in North America, ARs have significant surface hy-
64 drometeorological effects on the western North America (e.g., Ralph et al., 2006; Neiman
65 et al., 2008; Leung & Qian, 2009; Ralph et al., 2011; Dettinger, 2011; Rutz et al., 2014;
66 X. Chen et al., 2018) and the US Midwest (e.g., Lavers & Villarini, 2013; Nayak & Vil-
67 larini, 2017).

68 The first and critical task to study ARs is to develop AR identification methods.
69 There have been many AR detection and tracking methods for different purposes in the
70 literature, as noted in the Atmospheric River Tracking Method Intercomparison Project (ARTMIP,
71 Shields et al., 2018; Rutz et al., 2019; O'Brien et al., 2020). These different detection meth-
72 ods are primarily based on either one or both measurements of Integrated Water Vapor
73 (*IWV*) and Integrated Water Vapor Transport (*IVT*).

74 Ralph et al. (2004, 2005, 2006) created an objective AR identification method us-
75 ing satellite-based *IWV* for case studies in the North American West Coast. They de-
76 fined ARs with *IWV* content > 20 mm, length > 2000 km, and width < 1000 km. Sim-

ilar approaches have since been widely applied (e.g., Neiman et al., 2008; Wick et al., 2013). Furthermore, *IVT* derived from reanalysis or models incorporates the effects of advection. Zhu and Newell (1998) first defined ARs through *IVT*. Lavers et al. (2012) and Lavers and Villarini (2013), respectively, established percentile-based *IVT* thresholds to study ARs affecting Britain and Central US. Guan and Waliser (2015) applied 85th percentile seasonal climatological thresholds to *IVT* for global AR detection. Meanwhile, Rutz et al. (2014) used absolute thresholds, preferring $IVT \geq 250 \text{ kg m}^{-1} \text{ s}^{-1}$ to $IWV \geq 20 \text{ mm}$ as a threshold to emphasize inland-penetrating ARs in the Western US.

IVT-based detection method is increasingly chosen over *IWV*-based ones in research and operation as horizontal moisture transport is qualitatively related with orographic precipitation (e.g., Neiman et al., 2009; Rutz et al., 2014; Guan & Waliser, 2015). The combination of *IVT* and *IWV* (*IVT+IWV* thereafter) was recently adopted (e.g., Eiras-Barca et al., 2016; Gershunov et al., 2017). The *IVT + IWV* method was proposed to reduce erroneous detection of ARs from considering only one of the measurements (Eiras-Barca et al., 2016). It requires both *IVT* and *IWV* values to meet their corresponding thresholds simultaneously.

Furthermore, the duration of an AR is important for its hydrometeorological effects. Longer-lived ARs are more likely to bring higher rainfall (in total and on average) and streamflow than shorter-duration ones (Ralph et al., 2013; Nayak & Villarini, 2018). However, there has not been a consensus in duration criteria. Duration thresholds were not used in some early case studies (e.g., Ralph et al., 2004). Subsequently, a minimum of at least 8 (Ralph et al., 2013), 12 (Payne & Magnúsdóttir, 2016), 18 (Lavers et al., 2012; Lavers & Villarini, 2013; Nayak & Villarini, 2017; Gershunov et al., 2017), or 24 consecutive hours (Sellars et al., 2015) were included as a part of detection algorithms.

Although systematic comparisons among different AR identification methods are underway (Shields et al., 2018; Rutz et al., 2019; Ralph et al., 2019), the relationships between the methods and associated AR precipitation remain to be quantified. Important questions to ask include: between the two common detection measurements of *IVT* and *IWV*, which one, or both, should be used when surface precipitation is concerned? How do more restrictive duration criteria perform if long-lived ARs produce larger amounts of precipitation than short-lived ones (Ralph et al., 2013)? In probing these questions, we attempted to establish an optimal AR detection algorithm suited for expressing sur-

109 face precipitation impacts. We used a multi-factorial ensemble analysis, well suited for
 110 uncertainty quantification, focusing on the percentile-based approaches within the ART-
 111 MIP framework of prevailing detection methods and reanalysis data from January 1980
 112 to June 2017. The paper is organized as follows: data and methods are in section 2. Sur-
 113 face precipitation effects associated with different AR detection indices are analyzed and
 114 discussed in section 3. Sections 4 and 5 provide discussions and conclusions, respectively.

115 2 Data and Methods

116 2.1 Data

117 2.1.1 MERRA-2 data for ARTMIP

118 The two conventional moisture measurements for AR detection, IVT and IWV ,
 119 were extracted from the Modern-Era Retrospective analysis for Research and Applica-
 120 tions, Version 2 (MERRA-2) source data for ARTMIP through Climate Data Gateway (NCAR
 121 CDG, 2019). This dataset was calculated by the Center for Western Weather and Wa-
 122 ter Extremes at the University of California, San Diego, according to the following for-
 123 mula (Shields et al., 2018):

$$124 \quad IVT = -\frac{1}{g} \int_{1000}^{200} q(p) |\mathbf{V}_h(p)| dp, \quad (1)$$

$$125 \quad IWV = -\frac{1}{g} \int_{1000}^{200} q(p) dp \quad (2)$$

126 The three variables, horizontal wind ($\mathbf{V}_h = (u, v)$ where u is the zonal and v the
 127 meridional winds in m s^{-1}), specific humidity (q in kg kg^{-1}), and pressure (p in hPa),
 128 used in the formula were from NASA MERRA-2 (Gelaro et al., 2017). The horizontal
 129 spatial resolution and temporal resolution of the vertically integrated fields are 0.5° lon-
 130 gitude by 0.625° latitude and 3 hours. We used all of the MERRA-2 Tier 1 data avail-
 131 able at the time of download, from January 1980 to June 2017, to create climatological
 132 thresholds. Then, we applied the AR detection algorithm to the dataset to generate AR
 133 indices.

2.1.2 CPC US Unified Precipitation Data

The NOAA Climate Prediction Center (CPC) Unified Gauge-Based Analysis of Daily Precipitation over the Contiguous United States (hereafter, CPC) provides daily precipitation on a fine-resolution (0.25° latitude by 0.25° longitude) from January 1948 to the present (Higgins et al., 2000; Xie et al., 2007; M. Chen et al., 2008). Gibson et al. (2019) evaluated this product and found overall good agreement with the in-situ Parameter-Elevation Regressions on Independent Slopes Model (PRISM) dataset (Daly et al., 2008). We used data downloaded from the NOAA CPC website (NOAA/OAR/ESRL PSL, 2021) to investigate the surface precipitation effects of the AR indices. As described in the next subsection, these AR indices were defined by various AR detection criteria applied to the ARTMIP MERRA-2 data. Their original spatial and temporal resolutions are those of the MERRA-2. We spatially interpolated the coarser AR index values (0 or 1) with bilinear interpolation to the CPC data’s finer mesh, then rounded off the results to integers. Each CPC daily precipitation measurement was divided evenly over the twenty-four hours centered at 00 UTC, then aggregated into the AR indices’ 3-hourly intervals.

2.2 AR Detection Algorithm

As shown in Figure 1, we used 4 factors—moisture fields, climatological thresholds, shape criteria, and temporal thresholds—to generate an ensemble of 81 AR indices for the US West Coast and 81 for the Midwest. First, we used IVT , IWV , or $IVT+IWV$ as the moisture field. Then, for each grid point, we selected moisture field values at 1200 UTC every day during neutral or weak El Niño–Southern Oscillation (ENSO) events from January 1980 to June 2017. We called these test values. Here, we adopted the bi-monthly NOAA Multivariate ENSO index (MEI.v2, e.g., Wolter & Timlin, 1993) and preserved only test values in the months when the MEI.v2 index was within ± 1 . Three monthly climatological thresholds were calculated for each set of test values— IVT , IWV , or $IVT+IWV$ —at each grid point. In addition to the common 85th percentile (e.g., Lavers et al., 2012; Lavers & Villarini, 2013; Guan & Waliser, 2015; Eiras-Barca et al., 2016), we also used the 75th and the 95th percentiles as thresholds. Consequently, at any given grid point and time, a moisture value equal to or exceeding a threshold suggests the potential presence of AR.

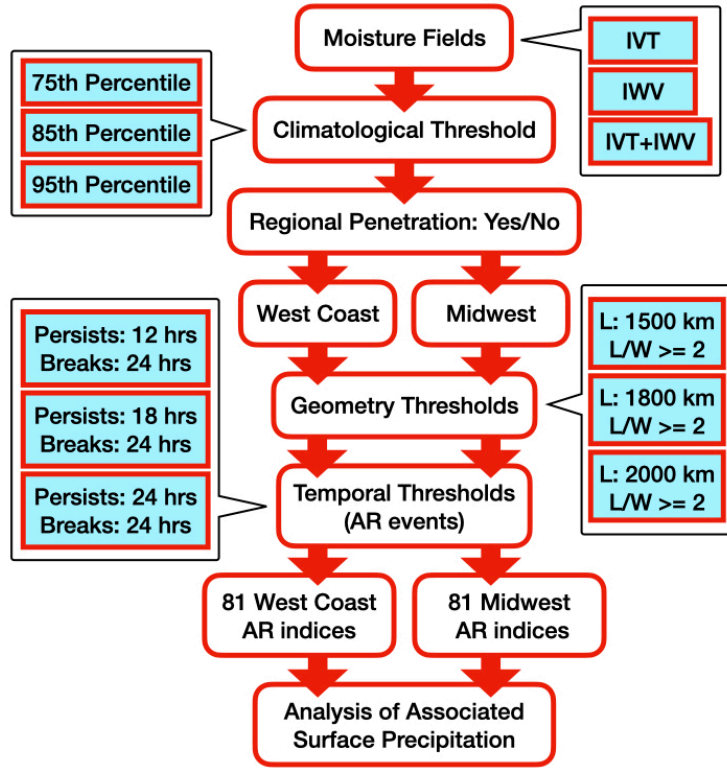


Figure 1. Schematic diagram illustrating the multifactorial AR detection algorithm.

165 Figure 2 plots these three levels of climatological thresholds of *IVT* and *IWV* fields
 166 over North America for January and August. The threshold at each grid point elevates
 167 successively, increasingly restricting AR detection, from 75th to 95th percentile. The *IVT*
 168 maxima corresponded to extratropical storm tracks and ITCZ over the North Pacific and
 169 the North Atlantic. The *IWV* maxima co-located with tropical and extratropical warm
 170 oceans as well as maritime tropical air mass. Consistent with Clausius–Clapeyron equa-
 171 tion, *IVT* and *IWV* thresholds were generally higher in the summer (August) than in
 172 the winter (January). To relate identified ARs with surface precipitation effects, we de-
 173 fined the regions of West Coast and Midwest based on the boundaries of CPC precip-
 174 itation data. The regions of the West Coast (situating between 33°–48.5° N and 124.375°–
 175 114.375° W) and Midwest (between 37°–47° N and 94°–84° W) are outlined in red. This
 176 seasonal difference was more evident in the Midwest than the West Coast. Regardless,
 177 the *IVT* maximum over the Northeast Pacific Ocean expanded towards the West Coast
 178 in January, then retreated in August.

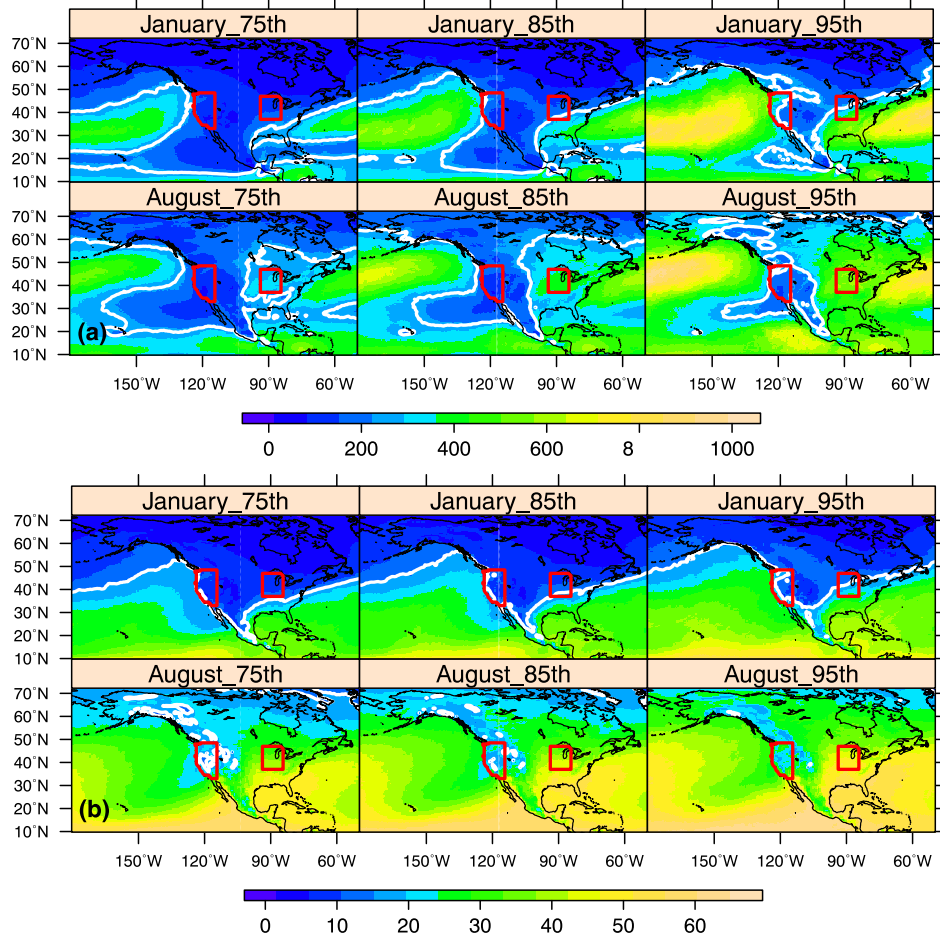


Figure 2. Three levels (75th, 85th, and 95th) of climatological thresholds of IVT (a, $\text{kg m}^{-1}\text{s}^{-1}$) and IWV (b, kg m^{-2}) over North America for January and August derived from neutral or weak ENSO events between January 1980–June 2017. The red boxes outline the West Coast and Midwest regions in this study. White lines ($250 \text{ kg m}^{-1}\text{s}^{-1}$ in IVT and 15 kg m^{-2} in IWV) are the absolute thresholds in Gereshunov et al. (2017).

179 Figure 2 also compares the monthly percentile thresholds in this study against the
 180 absolute thresholds used by Gershunov et al. (2017), defined as $250 \text{ kg m}^{-1}\text{s}^{-1}$ in *IVT*
 181 and 15 kg m^{-2} in *IWV*. The monthly percentile thresholds exhibit more spatial details
 182 as well as seasonal variability than the absolute ones. Through visual inspection, one can
 183 infer the different outcomes of AR detection if solely based on these thresholds. In Jan-
 184 uary, absolute *IVT* and *IWV* thresholds resulted in fewer instances of landfalling ARs
 185 in both West Coast and Midwest compared with the respective 75th and 85th percentile
 186 thresholds. This is because the majority of the monthly percentile threshold values in
 187 these two regions are below the absolute thresholds. The absolute thresholds, however,
 188 permitted more frequent January AR detection along the West Coast and southern Mid-
 189 west than the 95th percentile threshold values. These were also true for West-Coast AR
 190 detection using *IVT* in August; however, in the Midwest, the absolute *IVT* threshold
 191 was less restrictive to August AR detection than all *IVT* monthly percentiles. The ab-
 192 solute *IWV* threshold allowed overall more August AR detection than the monthly per-
 193 centiles in the plotted domain.

194 The variability of AR detection across various thresholds above attests to the ne-
 195 cessity of additional constraints. At each time step, we identified the grid points whose
 196 *IVT* or *IWV* values exceeded their corresponding climatological thresholds and kept only
 197 the data of those making landfall in the West Coast or penetrating into the Midwest.
 198 Then, we used the principal curves method (Hastie & Stuetzle, 1989) to determine the
 199 length of the curvy patterns formed by aggregating the maximum *IVT* or *IWV* values
 200 at each latitude and longitude. The width was calculated as the total Earth surface area
 201 of the identified grid points divided by the length. The geometry thresholds were fur-
 202 ther applied. A subset of potential AR data was extracted if a length was greater or equal
 203 to 1500, 1800, or 2000 km while the ratio of length to width was greater or equal to 2
 204 (Figure 1). It is noted that, for the detection of West Coast land-falling ARs, this length
 205 was estimated using only the segment of data over the Pacific; for the ARs penetrating
 206 into the Midwest, it was estimated using the entire segment. The subsets of data were
 207 further filtered and aggregated into AR events that persisted for equal to or more than
 208 12, 18, or 24 hours with breaks shorter than 24 hours within an event. The length of break
 209 criterion was based on Lavers and Villarini (2013).

210 At this point, 81 members of AR indices for each of the West Coast and Midwest
 211 regions from January 1980 to June 2017 were completed. Each index identifies the spa-

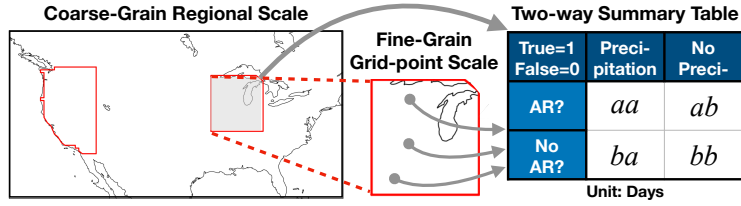


Figure 3. A two-way summary table with the terms for evaluating AR indices' relationships with surface precipitation on coarse- and fine-grain scales.

212 tial and temporal information of AR events that satisfied one of the 81 combinations of
 213 the criteria form by the four factors. We proceeded with systematic analysis of the re-
 214 lationships between these ARs and surface precipitation in the West Coast and the Mid-
 215 west. The AR detection and detailed analysis were executed via distributed-parallel com-
 216 puting on a high-performance computing cluster with Hadoop system in the backend and
 217 the R language-based DeltaRho software in the frontend (Cleveland & Hafen, 2014; Tung
 218 et al., 2018).

219 2.3 Coarse- to Fine-Grain Two-Way Summary Table

220 We built a two-way summary table (Figure 3) to explore the relationships between
 221 ARs identified by the indices and the surface precipitation in the West Coast and the
 222 Midwest. We took two spatial scales into account: regional coarse-grain scale and grid-
 223 point fine-grain scale. On the coarse-grain scale, we regarded either West Coast or Mid-
 224 west as one entity. Within each entity, days centered at 00 UTC with at least one AR
 225 time step identified in a 3-hourly AR index were defined as AR days. Days without any
 226 AR time steps were considered as no AR days. Precipitation was based on the CPC US
 227 Unified Precipitation Data. The *aa* in the summary table was total AR days with pre-
 228 cipitation; the *ab* was AR days without precipitation; the *ba* was days with no ARs but
 229 with precipitation; and the *bb* was days with no ARs and no precipitation.

230 From the summary table, four statistics were derived: *AR Related Precipitation*,
 231 *Precision*, *Accuracy*, and *F1 score*. The names loosely follow those in statistical classi-
 232 fication (e.g., Hastie et al., 2001). However, the statistics here did not validate any pre-
 233 dictive modeling of precipitation. They were used to compare the MERRA-2 AR indices'
 234 performance of relating to CPC surface precipitation effects. They may, however, pro-

235 vide empirical upper limits of a predictive model using only an AR index to predict pre-
 236 cipitation within the data, spatial, and temporal domains in the study. *AR Related Pre-*
 237 *cipitation* is defined as

$$238 \quad \frac{aa}{aa + ba} = \frac{aa}{D_P}, \quad (3)$$

239 with D_P the total days with precipitation. It specifies how often surface precipitation,
 240 if existed, was related to the ARs identified by an index. In predictive modeling, *AR Re-*
 241 *lated Precipitation* is called *Sensitivity* in statistics or *Probability of Detection* in weather
 242 forecast. *Precision* is defined as

$$243 \quad \frac{aa}{aa + ab} = \frac{aa}{D_{AR}}, \quad (4)$$

244 with D_{AR} the total days with ARs according to an index. It describes how often the de-
 245 tected ARs were actually related with precipitation. In weather forecast, *Precision* equals
 246 to 1-*False Alarm Ratio*. *Accuracy* is defined as

$$247 \quad \frac{aa + bb}{aa + ab + ba + bb} = \frac{aa + bb}{D}, \quad (5)$$

248 with D the total 13695 days in the data. For each AR index, it measures how often days
 249 with/without ARs were correctly associated with precipitation/no precipitation. The *F1*
 250 *score*,

$$251 \quad \frac{2 * AR \text{ Related Precipitation} * Precision}{AR \text{ Related Precipitation} + Precision}, \quad (6)$$

252 is the harmonic mean of *AR Related Precipitation* and *Precision*. An AR index with a
 253 low *F1 score* has both poor *AR Related Precipitation* and poor *Precision*, therefore an
 254 overall poor AR-precipitation relation.

255 Each of these four statistics had one resultant value for each index on the coarse-
 256 grain scale in either West Coast or Midwest. On the fine-grain scale, they were multi-
 257 plied by the number of grid points inside a region: 2069 in the West Coast and 1508 in
 258 the Midwest. The different sample sizes were taken into account in interpreting the re-
 259 sults (section 3.2).

260 **3 Analysis and Results**

261 **3.1 Identified AR occurrence summary statistics**

262 Figures 4 and 5 visualize three summary statistics of AR occurrence obtained with
 263 162 AR indices. These figures are Cleveland dotplots (Cleveland & McGill, 1984) cre-

264 ated in the Trellis display framework (Becker et al., 1996). The number of AR events
 265 (Figure 4a), the accumulated time of these events measured in 3-hourly time steps (Fig-
 266 ure 4b), and the average duration per event in days (Figure 5) are plotted on each panel,
 267 conditional on 18 combinations of regions (West Coast or Midwest), moisture fields (IVT ,
 268 IWV , or $IVT+IWV$), and AR length criteria (1500, 1800, or 2000 km). The results
 269 are 18 packets, or subsets, of values. Each packet has 9 paired values of a summary statis-
 270 tic in the y -axis and one of the AR persistent duration thresholds (12, 18, or 24 hours
 271 along the x -axis), grouped with color by climatological thresholds (75th, 85th, or 95th
 272 percentiles).

273 Figure 4a shows that, from January 1980 to June 2017, each 75th and 85th per-
 274 centile climatological threshold-based AR index captured $O(1000)$ events in either West
 275 Coast or Midwest regions, except for a few $IVT+IWV$ -based ones with the most re-
 276 strictive combinations of length and persistent duration criteria in the West Coast. In
 277 Figures 4b and 5, IWV -based indices identified the most AR time steps and longest av-
 278 erage per-event duration; $IVT+IWV$ -based indices identified the least and the short-
 279 est. Note that the per-event duration of each AR event was calculated as the summa-
 280 tion of persistent AR time segments, excluding the break times. Increasing the restric-
 281 tiveness of climatological threshold from 75th to 95th percentile while holding other fac-
 282 tors constant, the number of identified AR time steps decreased dramatically, so did the
 283 average duration per event.

284 However, more restrictive climatological thresholds did not always yield fewer AR
 285 events (Figure 4a). Among IVT - and IWV -based Midwest AR indices, the 85th per-
 286 centiles permitted more AR events but fewer time steps than the 75th percentiles, ow-
 287 ing to the latter’s tendency to yield longer per-event durations (Figure 5). Furthermore,
 288 the identified Midwest ARs had overall more total time steps than that of West-Coast
 289 ARs (Figure 4b). Midwest ARs had longer average per-event durations than those in the
 290 West Coast; the differences were the largest at the 75th percentiles and the least at the
 291 95th percentiles (Figure 5).

292 In Figures 4 and 5, the effects of length criteria were only secondary to climato-
 293 logical thresholds. However, increasing the thresholds of AR persistent duration from
 294 12 to 24 hours resulted in shorter accumulated time steps (Figure 4b) and, in most cases,

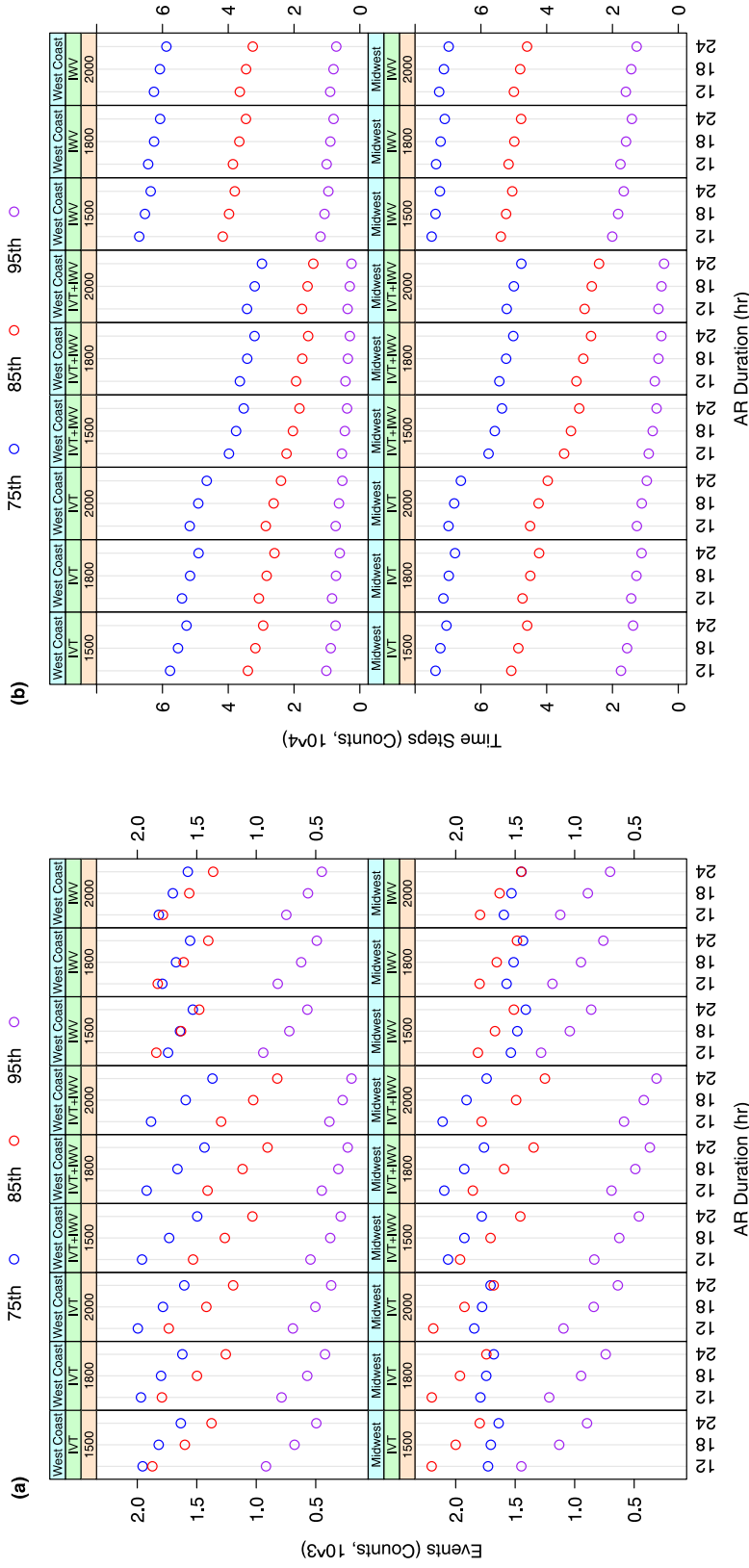


Figure 4. Numbers of (a) AR events (counts) and (b) accumulated AR time steps (counts) identified by 81 West-Coast (top row) and 81 Midwest (bottom row) AR indices. Each figure has 18 packets, or subsets of values conditional on 18 combinations of regions (West Coast or Midwest in blue boxes), moisture fields (IWT , IWV , or $IWT + IWV$ in green boxes), and AR length criteria (1500, 1800, or 2000 km shown in yellow boxes). Each packet has 9 paired values of a summary statistic in the y-axis and one of the AR persistent duration criteria (12, 18 and 24 hours along the x-axis), grouped by color into three levels of climatological thresholds (75th, 85th, and 95th percentiles shown respectively in blue, red, and purple).

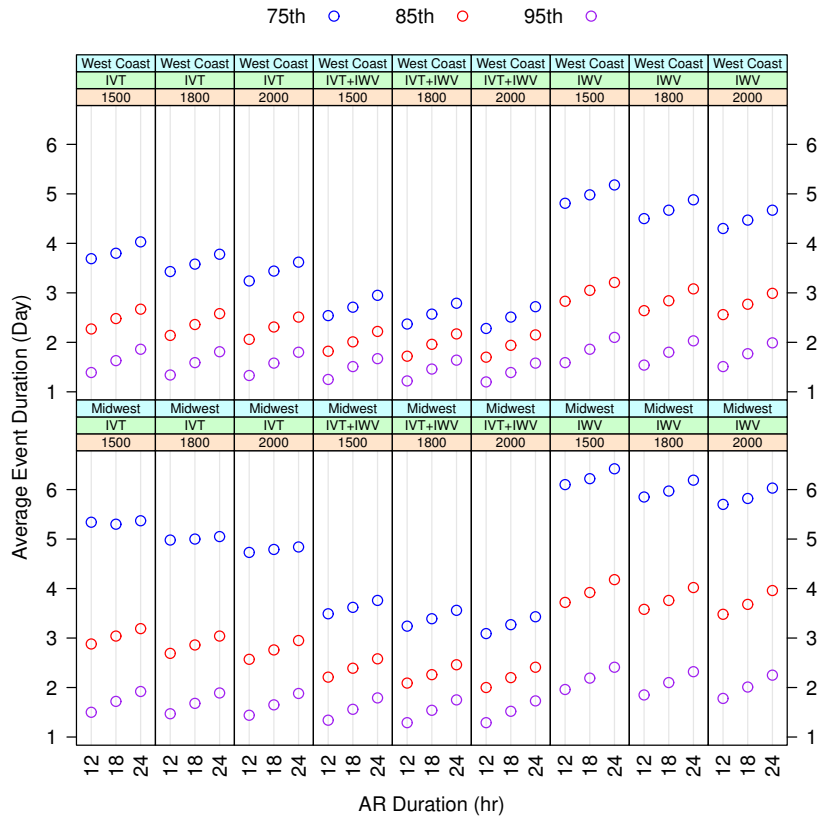


Figure 5. Similar to Figure 4, but for average per-event duration (unit: Day) identified by 81 West-Coast (top row) and 81 Midwest (bottom row) AR indices.

longer average per-event duration (Figure 5) of the identified ARs. It also led to decreasing AR event counts (Figure 4a).

3.2 Coarse- to fine-grain daily AR-precipitation occurrence relation analysis

3.2.1 Coarse-grain analysis

At the outset, we aimed to identify the AR indices that represent the precipitation occurrence as complete and correct as possible. Figure 6a shows the coarse-grain *Accuracy* in dotplots. An *Accuracy* of 1 means there was precipitation if and only if ARs were detected by an index. In general, indices associated with more AR time steps (Figure 4b) also exhibited higher *Accuracy* at the coarse-grain scale. Indeed, Midwest ARs bore higher *Accuracy* than the West Coast ARs given otherwise the same factors. The *IWV*-based AR indices yielded the highest *Accuracy* in both regions. Among them, indices using the 75th percentile climate threshold had *Accuracy* exceeding 0.64 in the West Coast and 0.74 in the Midwest. More restrictive climatological thresholds resulted in lower *Accuracy*. The lowest values were within the 95th-percentile-based *IVT + IWV* indices—below 0.09 for the West Coast and 0.14 for the Midwest ARs. More restrictive length and temporal criteria that detected fewer AR events or time steps also depressed *Accuracy* values, while the effect of length was minor in comparison to other factors.

Figure S1 shows the *AR Related Precipitation*, *i.e.*, the fraction of total days with precipitation attributable to identified ARs. It has a very similar pattern to Figure 6a. In particular, when 75th-percentile *IWV*-based indices were used, more than 64% and 74% of precipitation days occurred in the presence of ARs in the West Coast and Midwest, respectively. However, 95th-percentile *IVT+IWV*-based indices could only capture less than 9% and 14% of precipitation days in the respective regions. On the other hand, *Precision* values in Figure S2 display a very different pattern from Figures 6a or S1. For the West Coast landfalling ARs, 21 out of 81 indices had *Precision* equal to 1, with the rest approximately 1. That means each index very precisely associated AR days with precipitation. For ARs influencing the Midwest, the *Precision* values were slightly smaller but still larger than 0.998.

The *F1 scores* in Figure 6b summarizes for each AR index the combined performance of relating to the presence of precipitation (*Precision*) and explaining the occur-

326 rerence of precipitation (*AR Related Precipitation*) at the coarse-grain scale. Unlike *Ac-*
 327 *curacy*, *F1 score* does not consider days with no AR and no precipitation, expressed as
 328 the *bb* term in (5). In practice, we are more concerned about the relationship between
 329 the presence of AR and that of precipitation than the absence of both. Therefore, *F1*
 330 *score* is a more sensible measurement than *Accuracy*. Furthermore, the score could be
 331 considered as adjusted *Precision*, with which indices gained high *Precision* via narrow-
 332 ing to extreme samples are penalized. The adjustment differentiated the overall high *Pre-*
 333 *cision* values (Figure S2) to the pattern of *F1 scores* (Figure 6b), which resembles Fig-
 334 ures 6a and S1 but have larger magnitudes across the board.

335 **3.2.2 Fine-grain analysis**

336 We established for each index a two-way summary table for each individual grid
 337 point in West Coast and Midwest for fine-grain analysis. The distributions of fine-grain
 338 *F1 scores* are summarized using boxplots for the 81 West Coast AR indices, each with
 339 2069 points (Figure 7a) and 81 Midwest indices with 1508 points (Figure 7b).

340 In Figure 7a, the interquartile ranges (IQR) of the 81 *F1* distributions, as indicated
 341 by the box lengths, vary from ~ 0.017 to ~ 0.089 for the West Coast AR indices. Spa-
 342 tial inhomogeneity of precipitation captured by different indices contributed to this vari-
 343 ation. Another important influencer was the different AR days, D_{AR} , as inferred by the
 344 AR time steps (Figure 4b), resulted from different indices. Indeed, the smaller IQRs are
 345 seen among the most restrictive indices with the fewest AR time steps, such as the 95th-
 346 percentile *IVT + IWV*-based ones. Moreover, the minimum, first quartile (Q1), sec-
 347 ond quartile/median (Q2), third quartile (Q3), and maximum of each subset of *F1 scores*
 348 decrease with more restrictive criteria. This is consistent with the coarse-grain analy-
 349 sis (Figure 6b). When the climate threshold, length, and time criteria were fixed, the *IWV*-
 350 based indices slightly outperformed *IVT*-based ones and were significantly better than
 351 *IVT + IWV*-based ones. The 75th-percentile *IWV*-based indices yielded the largest
 352 median *F1 scores*, all exceeding 0.5.

353 The IQRs of fine-grain *F1 score* distributions for the 81 Midwest AR indices (Fig-
 354 ure 7b) are smaller than those for West Coast AR indices (Figure 7a). This is most cer-
 355 tainly due to the $\sim 30\%$ smaller sample size in the Midwest than that of the West Coast.
 356 The differences among the *F1 score* distributions in the Midwest are qualitatively sim-

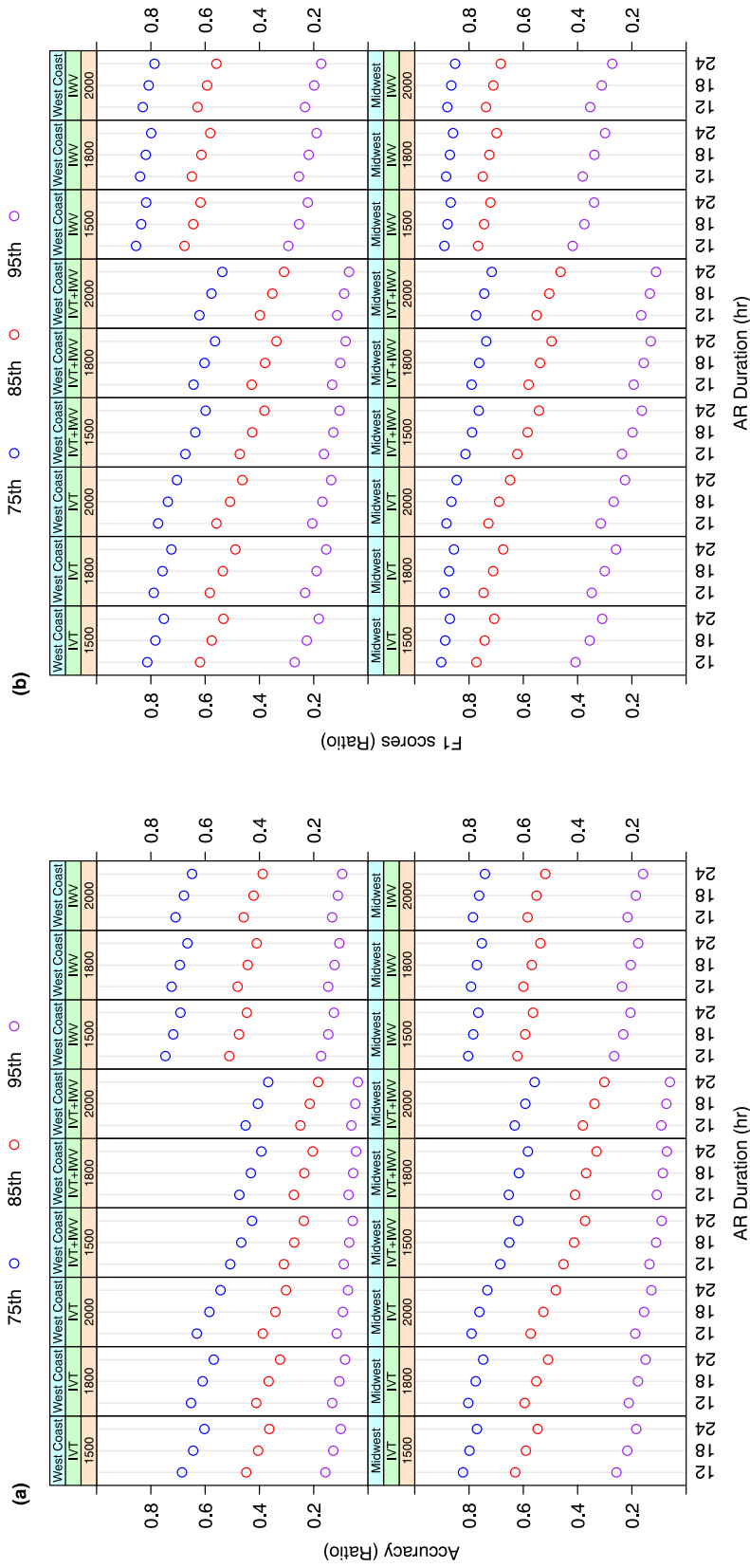


Figure 6. Similar to Figure 4, but for coarse-grain (a) Accuracy and (b) F1 scores for 81 West-Coast (top-row) and 81 Midwest (bottom-row) AR indices.

357 ilar to those in the West Coast. Nevertheless, the *F1 scores* in the Midwest are overall
 358 higher. The 75th-percentile *IWV*-based indices struck the highest median *F1 scores* at
 359 ~ 0.65 . These are consistent with the coarse-grain *F1* analysis (Figure 6b).

360 **3.3 Deep Analysis at the Finest Granularity**

361 In section 3.2, we studied the presence or absence of ARs in relation to those of pre-
 362 cipitation, as reflected by the ensembles of indices in the North American West Coast
 363 and the US Midwest. Past studies consistently showed that in general, ARs contributed
 364 to a fair amount of annual precipitation—up to 50% depending on the location—in the
 365 contiguous United States (Dettinger et al., 2011; Rutz & Steenburgh, 2012; Lavers & Vil-
 366 larini, 2015; Nayak & Villarini, 2017). Hence, in the next step, we analyzed the amount
 367 of AR-related precipitation associated with different indices. We quantified precipita-
 368 tion impacts with event-average rate (3.3.1) and event-accumulated precipitation (3.3.2
 369 and 3.3.3) and compared them across the AR indices.

370 ***3.3.1 Event-Average Surface Precipitation Effects***

371 For each AR index, we tracked the surface area of an AR at each recorded time step.
 372 We then calculated the areal-averaged surface precipitation rate at each time step. The
 373 event-average surface precipitation rate was calculated as the event time-mean of areal
 374 averages. As an example, Figure 8 compares the event-average precipitation rate across
 375 a group of AR indices with the 1500-km length and 18-hr persistent duration criteria us-
 376 ing boxplots, conditional on locations, climatological thresholds, and moisture fields. The
 377 values of precipitation rates shown are the original values plus one and transformed with
 378 base-2 logarithm to accommodate the wide range.

379 All indices for Midwest ARs in Figure 8 were prone to associate with more event-
 380 average precipitation than those for the West Coast ARs. As the climatological thresh-
 381 olds on moisture fields became increasingly more restrictive, the indices pointed to heav-
 382 ier event-average precipitation rates. One conspicuous feature in Figure 8 is that *IVT*+
 383 *IWV*-based indices are the strongest performer in both regions. As already shown in sec-
 384 tion 3.2, the combined moisture field posed the most restrictive criterion, detecting the
 385 fewest events with the shortest lifespan per event. The analysis further shows its propen-

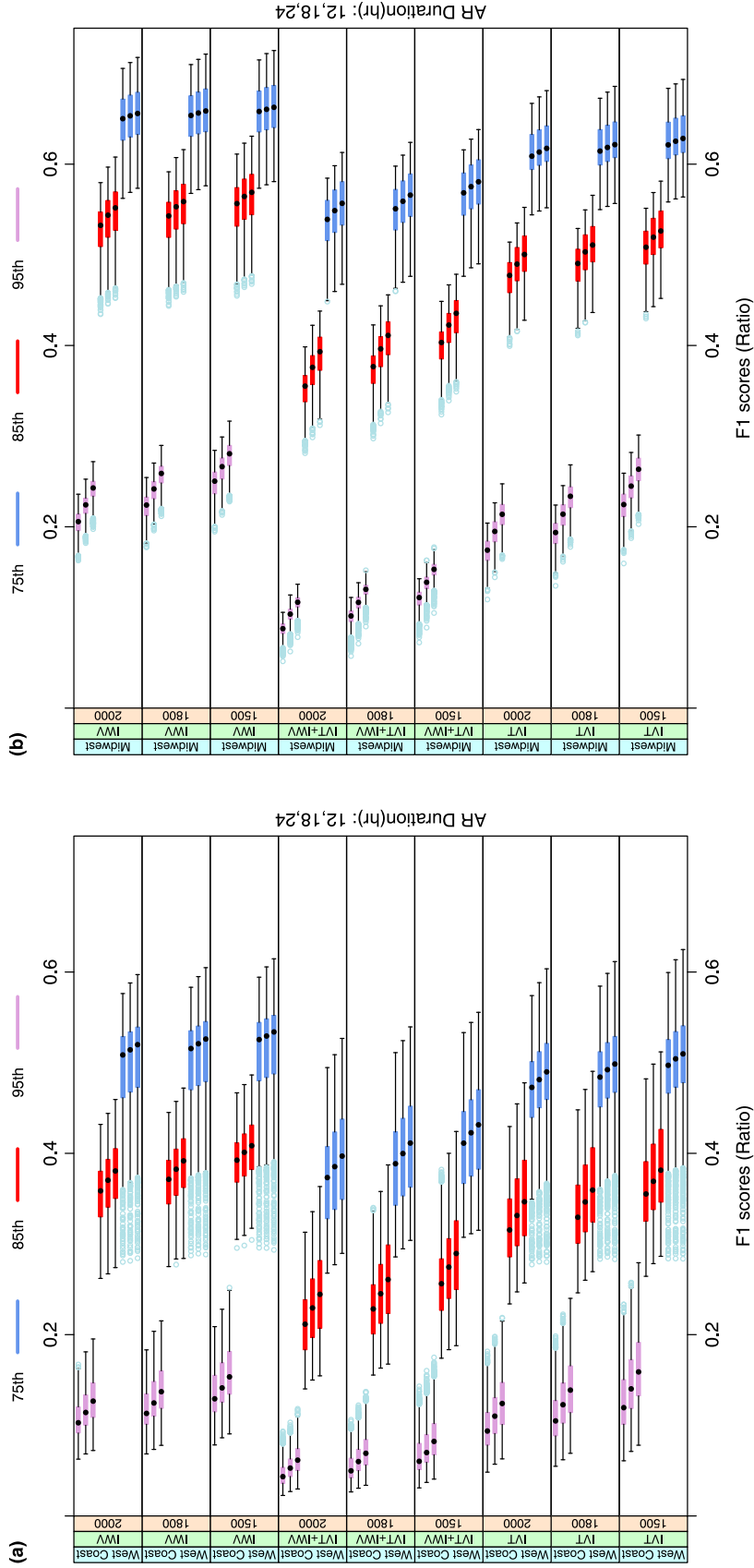


Figure 7. Boxplots of fine-grain $F1$ scores for the (a) West Coast and (b) Midwest AR indices. Each figure has nine packets from combinations of three moisture (IVT , IWV , or $IVT + IWV$) and three AR length criteria (1500, 1800, or 2000 km). Each packet has nine boxplots grouped by color into three levels of climatological thresholds (75th, 85th, or 95th percentile). Within each triplet, from bottom to top, the persistent duration thresholds increase from 12, 18, to 24 hours. Each boxplot includes the colored box spanning from $Q1$ to $Q3$ of the distribution, a black dot marking the median, and the whiskers. The whiskers extend to the most extreme data point that is no more than 1.5 times the length of the box (IQR) away from the box. Any data points outside the whiskers are marked as potential outliers in light blue.

386 sity to crop out AR features with the highest precipitation rates. This is consistent with
 387 previous studies (Neiman et al., 2008; Nayak & Villarini, 2018).

388 Another distinct feature in Figure 8 is the disparate performance of *IVT*-based in-
 389 dices between the West Coast and the Midwest. *IVT*-based AR indices were associated
 390 with higher event-average precipitation in the West Coast than *IWV*-based ones. How-
 391 ever, this was not the case in the Midwest. This difference is likely due to the orographic
 392 origin of precipitation on the West Coast. Compared with *IWV*, the horizontal trans-
 393 port of moisture expressed by the *IVT* better indicated the vertical lifting and conden-
 394 sation processes upon convergence at the coastal mountains' windward side. Notably,
 395 the 95th percentile *IVT*-based West Coast AR index captured the intense orographic
 396 precipitation that *IWV* missed.

397 The effects of shape and temporal criteria on the detected ARs' relations to event-
 398 average surface precipitation rate were inconclusive across different climatological thresh-
 399 olds and moisture fields (Figures S3 and S4). Overall, longer persistent duration crite-
 400 ria appeared to be associated with more average precipitation. Still, the climatological
 401 thresholds and moisture fields had the first-order influences on the event-average surface
 402 precipitation rate.

403 ***3.3.2 Deep Analysis of Accumulated Precipitation at Fine Granular-*** 404 ***ity***

405 Although the event-average surface precipitation is a useful metric for an AR in-
 406 dex's overall precipitation intensity, it is even more indicative of an AR's hydrometeo-
 407 rological impact when combined with total event duration. Therefore, we further quan-
 408 tified such hydrometeorological impact using event-accumulated precipitation averaged
 409 inside a surface area swept by a detected AR. We defined, for each AR index, this area
 410 with all grid points visited at least once by the detected AR throughout its lifetime within
 411 the West Coast or Midwest region (shown in Figure 9). Given this area, we calculated
 412 the areal average of precipitation at each time step, then summed through all time steps
 413 to obtain event-accumulated precipitation for the AR event.

414 Figures S5 and S6, respectively, show the swept-area distributions resulted from
 415 West Coast and Midwest AR indices. The area of the West Coast region is about 1.38
 416 times that of the Midwest region, as shown by the data upper bounds in these figures.

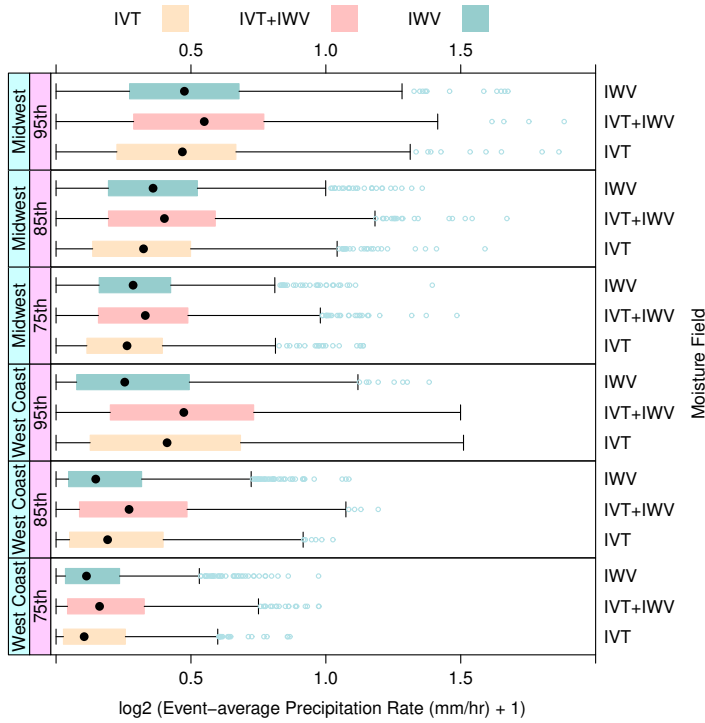


Figure 8. Boxplots of base-2 logarithmic transformation of event-average precipitation rate plus 1 (in mm hr⁻¹) over unit area according to *IVT*, *IVT + IWV*, and *IWV*-based AR indices with the same 1500-km length and 18-hr persistent duration criteria, conditional on locations and climatological thresholds labeled as percentile in 75th, 85th, and 95th.

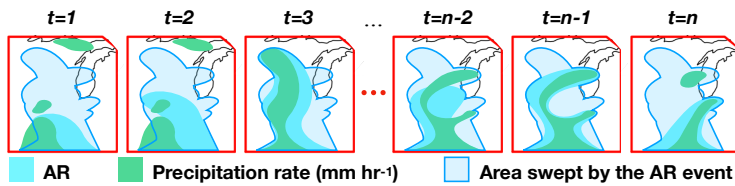


Figure 9. Schematic interpretation of spatial-averaged granule-level AR event-accumulated precipitation.

417 As expected, these areas decreased with increasing climatological thresholds; the areas
 418 increased with more restrictive persistent duration thresholds; $IVT + IWV$ -based in-
 419 dices restricted the areas to the smallest among all moisture fields, other factors being
 420 equal. Using the 75th percentile climatological thresholds, IWV -based indices tended
 421 to sweep a slightly broader area than IVT -based ones. In the Midwest region, the me-
 422 dian areas of the 75th-percentile IWV -based AR indices were identical to the area up-
 423 per bound; at least 50%—but fewer than 75%—of the AR events covered the entire Mid-
 424 west region. The 75th-percentile IVT -based AR indices had median areas smaller than
 425 but very close to this upper bound. However, the areal differences between IWV - and
 426 IVT -based indices diminished at 95th percentile thresholds.

427 Figure 10a compares the event-accumulated precipitation per unit area, plus one
 428 and transformed with base-2 logarithm, across the 81 West Coast AR indices using box-
 429 plots. The IQRs straddle one order of magnitude, with medians at ~ 3 –10 mm and Q3s
 430 reaching as high as ~ 16 mm. The climatological and persistent duration thresholds af-
 431 fected the resultant accumulated precipitation the most. We see that the more restric-
 432 tive duration thresholds retained higher accumulated precipitation events when other
 433 factors were fixed. The effects of changing the climatological thresholds, however, are
 434 not as simple.

435 The AR indices based on the 75th percentile IWV performed as well as, if not bet-
 436 ter than, any other 75th percentile indices in the West Coast region. Increasing the cli-
 437 matological threshold of IWV beyond this point did not necessarily increase accumu-
 438 lated precipitation (Figure 10a). Since the area swept by the ARs decreased (Figure S5)
 439 and the event-average precipitation likely increased (e.g., Figure 8), the shorter event du-
 440 ration (Figure 5) was responsible for this decline in accumulated precipitation. However,
 441 among the IVT - and $IVT + IWV$ -based indices, increased climatological thresholds
 442 resulted in increased event-accumulated precipitation (Figure 10a). Even so, the event
 443 duration decreased (Figure 5). Again, this could be attributed to the orographic effect
 444 on intense precipitation, a prominent influencer of accumulated precipitation retained
 445 by IVT and $IVT + IWV$ but missed by IWV with restrictive climatological thresh-
 446 olds. IVT 's prowess in capturing the accumulated precipitation stands out with the 95th-
 447 percentile threshold, considering that 95th-percentile IVT - and IWV -based indices swept
 448 over similar sizes of areas (Figure S5), and IVT indices tended to have shorter event du-
 449 ration than IWV ones (Figure 5).

450 Figure 10b compares the accumulated precipitation across the 81 Midwest AR in-
 451 dices using boxplots. In general, detected Midwest ARs tended to bring twice the amount
 452 of event accumulated precipitation than the West Coast ARs. The Q2s, or median val-
 453 ues, are at ~ 8 –16 mm and Q3s extending to ~ 30 mm. Similar to the West Coast AR
 454 indices, more restrictive persistent duration thresholds led to higher accumulated pre-
 455 cipitation. Different from the West Coast, indices based on *IWV* outperformed those
 456 based on *IVT* or *IVT + IWV* and resulted in the most accumulated precipitation in
 457 the Midwest across all climatological thresholds.

458 Moreover, increasing the climatological thresholds decreased accumulated precip-
 459 itation regardless of choices of moisture field. Comparison between Figures 10a and 10b
 460 shows that the choice of moisture field affected the detected AR’s accumulated precip-
 461 itation differently by region. AR indices with longer event duration (Figure 5) tend to
 462 be associated with more event-accumulated precipitation in the Midwest, whereas in-
 463 dices with larger event-average precipitation rate (Figure 8) are related to more precip-
 464 itation accumulation in the West Coast. This strongly suggests that the choice of mois-
 465 ture field for AR indices that best expresses surface precipitation impacts on a geograph-
 466 ical region ultimately depends on the physical understanding of the region’s precipita-
 467 tion processes.

468 ***3.3.3 Seasonal Effects on Event-Accumulated Precipitation***

469 Previous studies have demonstrated the seasonality of AR occurrence (Neiman et
 470 al., 2008; Lavers & Villarini, 2015; Nayak & Villarini, 2017). With seasonality as a point
 471 of departure, we further examined the event-accumulated precipitation. In particular,
 472 section 3.3.2 showed that the climatological threshold and moisture field choices for an
 473 AR index significantly affected its resultant accumulated precipitation. Figure 11, there-
 474 fore, compares the accumulated precipitation across a group of AR indices using box-
 475 plots conditional on locations, climatological thresholds, seasons, and moisture fields. For
 476 simplicity, only indices with 1500-km length and 18-hr persistent duration thresholds are
 477 shown.

478 Among landfalling West Coast ARs, there was a clear seasonal cycle in the accu-
 479 mulated precipitation that maximized in the winter and minimized in the summer. The
 480 phase of this seasonal cycle remained unchanged across all climatological thresholds. This

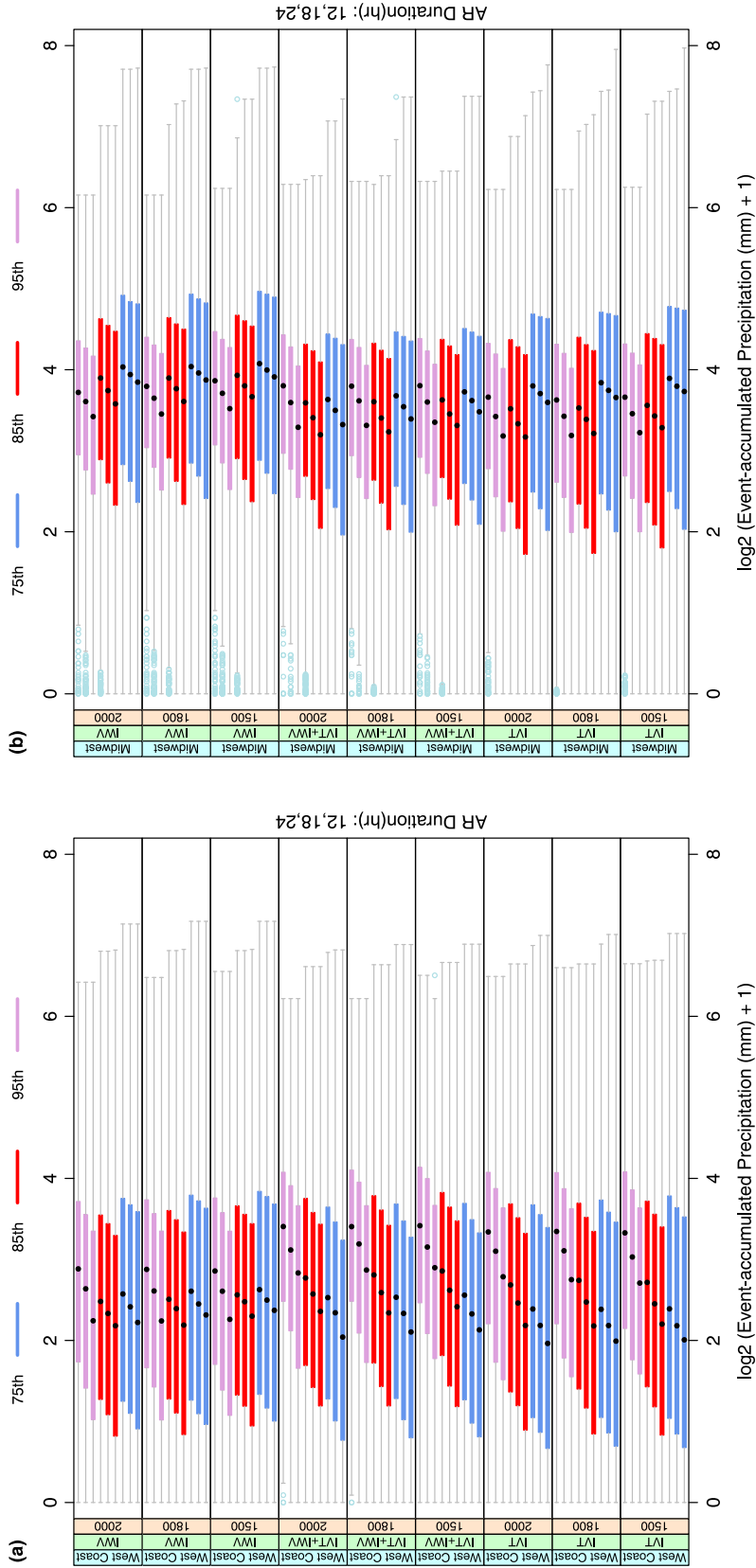


Figure 10. Boxplots of event-accumulated precipitation (mm) over unit area swept by ARs in the (a) West Coast and (b) Midwest. The results are base-2 logarithmic transformation of the original values plus 1, and are conditional on nine combinations of moisture fields (*IWT*, *IWV*, or *IVT* + *IWV*) and AR length criteria (1500, 1800, or 2000 km). Each resultant packet has nine boxplots grouped by color into three levels of climatological thresholds (75th, 85th, or 95th percentile). Within each triplet, from bottom to top, the persistent duration thresholds increase from 12, 18, to 24 hours.

481 is consistent with the rainy and dry seasons in the West Coast, as well as the previous
482 conclusion that warm seasons had less AR-related precipitation in the West Coast (Neiman
483 et al., 2008). Moreover, the combined effects of climatological threshold and moisture
484 field on the event-accumulated precipitation also had seasonality. In the warm spring and
485 summer, *IWV*-based indices with the 75th climatological threshold led to the most ac-
486 cumulated precipitation. While in the fall and winter, *IVT*-based indices with the 95th
487 threshold corresponded with the most precipitation accumulation. This was likely due
488 to the significant orographic enhancement during the landfall of winter ARs but not sum-
489 mer ARs that Neiman et al. (2008) found.

490 In contrast, among the Midwest ARs, as the climatological threshold increased,
491 the accumulated precipitation maxima shifted from the spring-summer to the fall, and
492 the amount in the winter increased. These suggest a dichotomy of synoptic systems as-
493 sociated with Midwest ARs: In addition to extratropical cyclones, the warm-month ARs
494 received a significant amount of precipitation from maritime tropical air masses. Unlike
495 in the West Coast, *IWV*-based Midwest AR indices were associated with the most me-
496 dian precipitation across all climatological thresholds and seasons.

497 4 Discussions

498 A single optimal AR detection algorithm expressing the surface precipitation im-
499 pacts does not exist. A hint of bifurcation in our analysis started in Figure 2, in which
500 the Midwest climate thresholds underwent a greater seasonal change than that of the
501 West Coast. In section 3.3, we further found that, with meandering south-north moun-
502 tain ranges in the West Coast, *IVT*-based detection algorithms captured the intense oro-
503 graphic precipitation better than the *IWV*-based ones. This is consistent with the trend
504 to use *IVT*-based detection algorithms (Guan & Waliser, 2015). However, in the Mid-
505 west, in the absence of prominent orographic lifting, *IWV*-based AR indices were as-
506 sociated with most event-average precipitation and event-accumulated precipitation.

507 Midwest ARs recruit moisture from tropical sources such as the Gulf of Mexico,
508 Caribbean Sea, subtropical eastern North Pacific, and the Atlantic coast of Central Amer-
509 ica (Dirmeyer & Kinter, 2009, 2010). The diverse sources complicate the ARs' charac-
510 teristics (Dirmeyer & Kinter, 2010). In section 3.3.3, the seasonality of event-accumulated
511 precipitation in the Midwest shifted its peak phase from warm to cold seasons along with

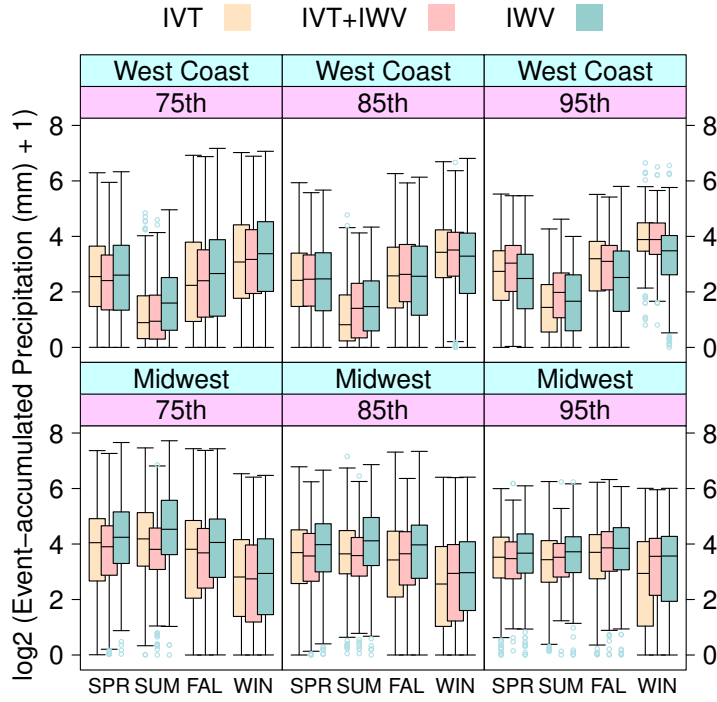


Figure 11. Boxplots of base-2 logarithmic transformation of event-accumulated precipitation (mm), plus 1, over unit area swept by AR in West Coast and Midwest during different seasons—spring (SPR: March–May), summer (SUM: June–August), fall (FAL: September–November), and winter (WIN: December–February)—according to *IVT*, *IVT+IWV*, and *IWV*-based AR indices with the 1500-km length and 18-hr persistent duration criteria, labeled as climate threshold in percentile 75th, 85th, or 95th in the purple box.

512 rising climate thresholds (Figure 11), suggesting a rolling change of moisture sources and
 513 baroclinicity as the seasons progressed. On the other hand, West Coast AR’s peak phase
 514 remained the same regardless of the changing climate threshold. There is a caveat, how-
 515 ever. The West Coast’s south-north geographic features are inhomogeneous. The land-
 516 falling AR characteristics between the Pacific Northwest and California coast are differ-
 517 ent in terms of occurrence frequency, occurrence time, and distribution and intensity of
 518 related precipitation (Neiman et al., 2008). Therefore, to further refine the AR detec-
 519 tion algorithms, the entire North American West Coast ARs could be divided into north-
 520 west and southwest ARs.

521 The combined *IVT+IWV*-based indices should be used cautiously. It is only the
 522 best of both worlds when the goal is to extract snapshots of extreme precipitating events.
 523 As seen in Figure 8, it led to the highest event-average precipitation rate in both West
 524 Coast and Midwest. This was, however, achieved through few and short events (Figures 4a,
 525 5). In fact, they performed the worst in AR–precipitation relation metrics such as *Accuracy*
 526 and *F1 scores* (Figures 6, 7).

527 Moreover, climate thresholds and moisture fields had first-order influences on the
 528 associated surface hydrometeorological impacts. However, more restrictive persistent du-
 529 ration thresholds can help obtain higher event-accumulated precipitation if that is the
 530 goal of detection (Figure 10).

531 Calculation of *IVT*-based indices requires height-dependent horizontal winds, so
 532 reanalysis data are indispensable. Previous studies have suggested that AR character-
 533 istics were robust across different reanalysis data (Nayak & Villarini, 2017; Ralph et al.,
 534 2019). We used MERRA-2 here since Nayak and Villarini (2017) recommended high-resolution
 535 products for AR impact assessments. Nevertheless, we showed that depending on the
 536 goal, *IWV* could provide optimal AR indices. When *IWV* is useful, researchers can use
 537 satellite or radiosonde water vapor measurements in lieu of reanalysis.

538 5 Conclusions

539 This paper investigated the optimal AR detection algorithm for expressing AR’s
 540 surface precipitation effects using the MERRA-2 data for ARTMIP. We applied a solution-
 541 driven approach by first asking which impacts, in which region, and in what time scale
 542 and period were of concern. We then used an algorithm combining climatological thresh-

543 olds, image processing, and statistical methods to create large ensembles of AR indices
 544 for answering the questions with uncertainty quantification aided by detailed data vi-
 545 sualization. Specifically, we varied the values of four factors—moisture fields, climato-
 546 logical thresholds, shape criteria, and duration thresholds—to generate an ensemble of
 547 81 AR indices for the US West Coast and 81 indices for the Midwest regions from 2006
 548 to 2015 (Figure 1). With CPC US Unified data, we examined the AR indices’ associa-
 549 tion with the surface precipitation impacts, including the daily co-occurrence (section
 550 3.2), event-average precipitation rate (section 3.3.1), and per-event accumulation (sec-
 551 tions 3.3.2 and 3.3.3).

552 The identified Midwest ARs had more accumulated time steps (Figure 4b), longer
 553 average per-event durations (Figure 5), more event-average precipitation (Figures 8, S3,
 554 and S4), and more event-accumulated precipitation (Figure 10) than the West Coast ARs.
 555 The results were sensitive to the selection of moisture field and climatological threshold
 556 in index generation. In West Coast and Midwest, *IWV*-based AR indices identified the
 557 most abundant AR event time steps and most accurately associated AR to days with
 558 precipitation. These were observed at the coarse-grain regional (Figure 6) and fine-grain
 559 grid-point scales (Figure 7). A restrictive climate threshold, such as the 95th percentile,
 560 emphasized extreme instances but limited event duration; therefore, it led to higher event-
 561 average precipitation rates. The most restrictive combination of 95th percentile *IVT*+
 562 *IWV*-based indices yielded the highest average precipitation (Figures 8, S5, and S6).

563 However, it is important to use both event-average and event-accumulated precip-
 564 itation as metrics for surface hydrometeorological impacts when scrutinizing the AR in-
 565 dices. Therefore, we defined an area swept by each AR event (Figures 9, S5, and S6) and
 566 calculated the event-accumulated precipitation per unit area for each AR index (Figure 10).
 567 On the West Coast, the 75th percentile *IWV*-based indices were associated with the most
 568 accumulated precipitation, while the 95th percentile *IVT* captured the accumulated pre-
 569 cipitation the best (Figure 10a). This could be explained by the *IVT*’s better represen-
 570 tation of intense coastal orographic precipitation. *IWV*-based AR indices with the longest
 571 persistent duration thresholds were associated with the most accumulated precipitation
 572 in the Midwest across a range of climate thresholds (Figure 10b). Therefore, we recom-
 573 mend to use *IWV*-based algorithm to identify AR-related surface precipitation in the
 574 Midwest but *IVT*-based algorithm to capture the orographically-induced precipitation
 575 in the West Coast.

576 Even more, the AR event-accumulated precipitation showed seasonality (Figure 11).
577 The accumulated precipitation of all West Coast landfalling ARs had a clear seasonal
578 cycle with the maximum in the winter and the minimum in the summer. However, for
579 the Midwest ARs, the phase of the seasonal cycle depended on the climatological thresh-
580 old. Increasing the climatological threshold from the 75th to the 95th percentile shifted
581 the maxima from the spring–summer to fall and accentuated winter precipitation; this
582 reflects the effects of seasonal change of moisture sources, convective instability, and at-
583 mospheric baroclinicity.

584 In conclusion, an optimal AR detection algorithm should be adaptive to the types
585 of impact to be addressed, the associated physical mechanisms in the affected regions,
586 timing such as the phase in the seasonal cycle, and event durations. The systematic en-
587 semble approach we used was made possible by distributed parallel computing with data
588 and, specifically, the divide-and-recombine approach using the R-based DeltaRho back-
589 ended by a Hadoop system. This study’s findings provide useful information for future
590 creators and users of AR indices who consider surface precipitation in their decision pro-
591 cesses. Our detection algorithms and computational approach can be applied to climate
592 model output, such as CMIP6, to explore the changes of ARs and AR-related surface
593 precipitation impacts in climate change scenarios.

594 **Acknowledgments**

595 The authors are grateful to R. Cannoodt, D. Crabill, Y. Song, M. Bowers and Purdue
596 ITAP RCAC for their help on computing with data. We are indebted to two anonymous
597 reviewers and the discussions with ARTMIP scientists, especially T. O’Brien, J. Rutz,
598 and C. Shields. We also thank W. L. Downing and C. Shen for insightful comments. Data
599 for this research are openly available through NCAR CDG (2019) and NOAA/OAR/ESRL
600 PSL (2021). AR indices further generated are available as Purdue data in NCAR CDG
601 (2021); special thanks to P. Ullrich for helping make the data available. The work is sup-
602 ported by DARPA-BAA-16-43-D3M-FP-051.

603 **References**

604 Becker, R. A., Cleveland, W. S., & Shyu, M. J. (1996). The visual design and con-
605 trol of trellis display. *Journal of Computational and Graphical Statistics*, 5(2),
606 123–155. doi: 10.1080/10618600.1996.10474701

- 607 Blamey, R. C., Ramos, A. M., Trigo, R. M., Tomé, R., & Reason, C. J. (2018).
 608 The influence of atmospheric rivers over the South Atlantic on winter rain-
 609 fall in South Africa. *Journal of Hydrometeorology*, *19*(1), 127–142. doi:
 610 10.1175/JHM-D-17-0111.1
- 611 Chen, M., Shi, W., Xie, P., Silva, V. B., Kousky, V. E., Higgins, R. W., & Janowiak,
 612 J. E. (2008). Assessing objective techniques for gauge-based analyses of
 613 global daily precipitation. *J. Geophys. Res. Atmos.*, *113*(4), 1–13. doi:
 614 10.1029/2007JD009132
- 615 Chen, X., Leung, L. R., Gao, Y., Liu, Y., Wigmosta, M., & Richmond, M. (2018).
 616 Predictability of Extreme Precipitation in Western U.S. Watersheds Based on
 617 Atmospheric River Occurrence, Intensity, and Duration. *Geophys. Res. Lett.*,
 618 *45*(21), 11,693–11,701. doi: 10.1029/2018GL079831
- 619 Cleveland, W. S., & Hafen, R. (2014). Divide and recombine (D&R): Data science
 620 for large complex data. *Statistical Analysis Data Mining*, *7*(6), 425–433. doi:
 621 10.1002/sam.11242
- 622 Cleveland, W. S., & McGill, R. (1984). Graphical perception: Theory, experimen-
 623 tation, and application to the development of graphical methods. *Journal of*
 624 *the American Statistical Association*, *79*(387), 531–554. doi: 10.1080/01621459
 625 .1984.10478080
- 626 Daly, C., Halbleib, M., Smith, J. I., Gibson, W. P., Doggett, M. K., Taylor, G. H.,
 627 ... Pasteris, P. P. (2008). Physiographically sensitive mapping of climatologi-
 628 cal temperature and precipitation across the conterminous United States. *Int.*
 629 *J. Climatol.*, *28*(15), 2031–2064. doi: <https://doi.org/10.1002/joc.1688>
- 630 Dettinger, M. D. (2011). Climate change, atmospheric rivers, and floods in Cal-
 631 ifornia - a multimodel analysis of storm frequency and magnitude changes.
 632 *Journal of the American Water Resources Association*, *47*(3), 514–523. doi:
 633 10.1111/j.1752-1688.2011.00546.x
- 634 Dettinger, M. D. (2013). Atmospheric rivers as drought busters on the U.S. West
 635 Coast. *Journal of Hydrometeorology*, *14*(6), 1721–1732. doi: 10.1175/JHM-D
 636 -13-02.1
- 637 Dettinger, M. D., Ralph, F. M., Das, T., Neiman, P. J., & Cayan, D. R. (2011). At-
 638 mospheric Rivers, Floods and the Water Resources of California. *Water*, *3*(2),
 639 445–478. doi: 10.3390/w3020445

- 640 Dirmeyer, P. A., & Kinter, J. L. (2009). The "Maya Express": Floods in the U.S.
641 Midwest. *EOS Transactions*, *90*(12), 101–102. doi: 10.1029/2009EO120001
- 642 Dirmeyer, P. A., & Kinter, J. L. (2010). Floods over the U.S. midwest: A regional
643 water cycle perspective. *Journal of Hydrometeorology*, *11*(5), 1172–1181. doi:
644 10.1175/2010JHM1196.1
- 645 Eiras-Barca, J., Brands, S., & Miguez-Macho, G. (2016). Seasonal variations in
646 North Atlantic atmospheric river activity and associations with anomalous pre-
647 cipitation over the Iberian Atlantic margin. *Journal of Geophysical Research*
648 *Atmosphere*, *121*(2), 931–948. doi: 10.1002/2015JD023379
- 649 Gelaro, R., McCarty, W., Suárez, M. J., Todling, R., Molod, A., Takacs, L., ...
650 Zhao, B. (2017). The modern-era retrospective analysis for research and ap-
651 plications, version 2 (MERRA-2). *Journal of Climate*, *30*(14), 5419–5454. doi:
652 10.1175/JCLI-D-16-0758.1
- 653 Gershunov, A., Shulgina, T., Ralph, F. M., Lavers, D. A., & Rutz, J. J. (2017).
654 Assessing the climate-scale variability of atmospheric rivers affecting west-
655 ern North America. *Geophysical Research Letters*, *44*(15), 7900–7908. doi:
656 10.1002/2017GL074175
- 657 Gibson, P. B., Waliser, D. E., Lee, H., Tian, B., & Massoud, E. (2019). Climate
658 model evaluation in the presence of observational uncertainty: Precipitation
659 indices over the contiguous United States. *Journal of Hydrometeorology*, *20*(7),
660 1339–1357. doi: 10.1175/JHM-D-18-0230.1
- 661 Guan, B., Molotch, N. P., Waliser, D. E., Fetzer, E. J., & Neiman, P. J. (2010).
662 Extreme snowfall events linked to atmospheric rivers and surface air temper-
663 ature via satellite measurements. *Geophysical Research Letters*, *37*(20). doi:
664 10.1029/2010GL044696
- 665 Guan, B., Molotch, N. P., Waliser, D. E., Fetzer, E. J., & Neiman, P. J. (2013).
666 The 2010/2011 snow season in California's Sierra Nevada: Role of atmospheric
667 rivers and modes of large-scale variability. *Water Resources Research*, *49*(10),
668 6731–6743. doi: 10.1002/wrcr.20537
- 669 Guan, B., & Waliser, D. E. (2015). Detection of atmospheric rivers: Evaluation and
670 application of an algorithm for global studies. *Journal of Geophysical Research*
671 *Atmosphere*, *120*(24), 12,514–12,535. doi: 10.1002/2015JD024257
- 672 Hastie, T., & Stuetzle, W. (1989). Principal Curves. *Journal of the American Statis-*

- 673 *tical Association*, 84(406), 502–516. doi: 10.1080/01621459.1989.10478797
- 674 Hastie, T., Tibshirani, R., & Friedman, J. (2001). *The elements of statistical Learn-*
675 *ing: Data mining, inference, and prediction*. Springer, New York, NY. doi: 10
676 .1007/978-0-387-84858-7
- 677 Higgins, R., Shi, W., Yarosh, E., & Joyce, R. (2000). *Improved United States precip-*
678 *itation quality control system and analysis*. NCEP/Climate Prediction Center
679 *ATLAS 7*.
- 680 Lavers, D. A., & Villarini, G. (2013). Atmospheric rivers and flooding over the cen-
681 tral United States. *Journal of Climate*, 26(20), 7829–7836. doi: 10.1175/JCLI
682 -D-13-00212.1
- 683 Lavers, D. A., & Villarini, G. (2015). The contribution of atmospheric rivers to pre-
684 cipitation in Europe and the United States. *Journal of Hydrology*, 522, 382–
685 390. doi: 10.1016/j.jhydrol.2014.12.010
- 686 Lavers, D. A., Villarini, G., Allan, R. P., Wood, E. F., & Wade, A. J. (2012). The
687 detection of atmospheric rivers in atmospheric reanalyses and their links to
688 British winter floods and the large-scale climatic circulation. *Journal of Geo-*
689 *physical Research Atmospheres*, 117(20). doi: 10.1029/2012JD018027
- 690 Leung, L. R., & Qian, Y. (2009). Atmospheric rivers induced heavy pre-
691 cipitation and flooding in the western U.S. simulated by the WRF re-
692 gional climate model. *Geophysical Research Letters*, 36(3), L03820. doi:
693 10.1029/2008GL036445
- 694 Little, K., Kingston, D. G., Cullen, N. J., & Gibson, P. B. (2019). The Role of
695 Atmospheric Rivers for Extreme Ablation and Snowfall Events in the Southern
696 Alps of New Zealand. *Geophysical Research Letters*, 46(5), 2761–2771. doi:
697 10.1029/2018GL081669
- 698 Luo, Q., & Tung, W.-w. (2015). Case study of moisture and heat budgets within at-
699 mospheric rivers. *Monthly Weather Review*, 143(10), 4145–4162. doi: 10.1175/
700 MWR-D-15-0006.1
- 701 Nayak, M. A., & Villarini, G. (2017). A long-term perspective of the hydroclimato-
702 logical impacts of atmospheric rivers over the central United States. *Water Re-*
703 *sources Research*, 53(2), 1144–1166. doi: 10.1002/2016WR019033
- 704 Nayak, M. A., & Villarini, G. (2018). Remote sensing-based characterization of rain-
705 fall during atmospheric rivers over the central United States. *Journal of Hy-*

- 706 *drology*, 556, 1038–1049. doi: 10.1016/j.jhydrol.2016.09.039
- 707 NCAR CDG. (2019). *3-hourly MERRA2 IVT, uIVT, vIVT, IWV data computed for*
- 708 *ARTMIP*. (last access: 24 January 2019) doi: 10.5065/D62R3QFS
- 709 NCAR CDG. (2021). *ARTMIP Tier 1 Catalogues*. (last access: 1 January 2021) doi:
- 710 10.5065/D6R78D1M
- 711 Neiman, P. J., Ralph, F. M., Wick, G. A., Lundquist, J. D., & Dettinger, M. D.
- 712 (2008). Meteorological characteristics and overland precipitation impacts of
- 713 atmospheric rivers affecting the West coast of North America based on eight
- 714 years of SSM/I satellite observations. *Journal of Hydrometeorology*, 9(1),
- 715 22–47. doi: 10.1175/2007JHM855.1
- 716 Neiman, P. J., White, A. B., Ralph, F. M., Gottas, D. J., & Gutman, S. I. (2009).
- 717 A water vapour flux tool for precipitation forecasting. *Proceedings of the Insti-*
- 718 *tution of Civil Engineers: Water Management*, 162(2), 83–94. doi: 10.1680/
- 719 wama.2009.162.2.83
- 720 NOAA/OAR/ESRL PSL. (2021). *CPC US Unified Precipitation*. (last access: 1 Jan-
- 721 uary 2021)
- 722 O’Brien, T. A., Payne, A. E., Shields, C. A., Rutz, J., Brands, S., Castellano, C., . . .
- 723 Zhou, Y. (2020). Detection uncertainty matters for understanding atmospheric
- 724 rivers. *Bulletin of the American Meteorological Society*, 101(6), E790–E796.
- 725 doi: 10.1175/bams-d-19-0348.1
- 726 Payne, A. E., & Magnusdottir, G. (2016). Persistent landfalling atmospheric rivers
- 727 over the west coast of North America. *Journal of Geophysical Research Atmo-*
- 728 *sphere*, 121(22), 13,287–13,300. doi: 10.1002/2016JD025549
- 729 Ralph, F. M., Coleman, T., Neiman, P. J., Zamora, R. J., & Dettinger, M. D.
- 730 (2013). Observed impacts of duration and seasonality of atmospheric-river
- 731 landfalls on soil moisture and runoff in coastal Northern California. *Journal of*
- 732 *Hydrometeorology*, 14(2), 443–459. doi: 10.1175/JHM-D-12-076.1
- 733 Ralph, F. M., Dettinger, M. D., Cairns, M. M., Galarneau, T. J., & Eylander, J.
- 734 (2018). Defining ”Atmospheric River”: how the glossary of meteorology helped
- 735 resolve a debate. *Bulletin of the American Meteorological Society*, 99(4),
- 736 837–839. doi: 10.1175/BMAS-D-17-0157.1
- 737 Ralph, F. M., Neiman, P. J., Kiladis, G. N., Weickmann, K., & Reynolds, D. W.
- 738 (2011). A multiscale observational case study of a Pacific atmospheric river

- 739 exhibiting tropical-extratropical connections and a mesoscale frontal wave.
740 *Monthly Weather Review*, 139(4), 1169–1189. doi: 10.1175/2010MWR3596.1
- 741 Ralph, F. M., Neiman, P. J., & Rotunno, R. (2005). Dropsonde observations in
742 low-level jets over the Northeastern Pacific Ocean from CALJET-1998 and
743 PACJET-2001: Mean vertical-profile and atmospheric-river characteristics.
744 *Monthly Weather Review*, 133(4), 889–910. doi: 10.1175/MWR2896.1
- 745 Ralph, F. M., Neiman, P. J., & Wick, G. A. (2004). Satellite and CALJET aircraft
746 observations of atmospheric rivers over the Eastern North Pacific ocean during
747 the winter of 1997/98. *Monthly Weather Review*, 132(7), 1721–1745. doi:
748 10.1175/1520-0493(2004)132<1721:SACAOO>2.0.CO;2
- 749 Ralph, F. M., Neiman, P. J., Wick, G. A., Gutman, S. I., Dettinger, M. D., Cayan,
750 D. R., & White, A. B. (2006). Flooding on California’s Russian River: Role
751 of atmospheric rivers. *Geophysical Research Letters*, 33(5), L13801. doi:
752 10.1029/2006GL026689
- 753 Ralph, F. M., Wilson, A. M., Shulgina, T., Kawzenuk, B., Sellars, S., Rutz, J. J.,
754 ... Wick, G. A. (2019). ARTMIP-early start comparison of atmospheric
755 river detection tools: how many atmospheric rivers hit northern California’s
756 Russian River watershed? *Climate Dynamics*, 52(7-8), 4973–4994. doi:
757 10.1007/s00382-018-4427-5
- 758 Rutz, J. J., Shields, C. A., Lora, J. M., Payne, A. E., Guan, B., Ullrich, P., ...
759 Viale, M. (2019). The Atmospheric River Tracking Method Intercomparison
760 Project (ARTMIP): Quantifying uncertainties in atmospheric river climatol-
761 ogy. *Journal of Geophysical Research: Atmospheres*, 124, 13,777–13,802. doi:
762 10.1029/2019JD030936
- 763 Rutz, J. J., & Steenburgh, W. J. (2012). Quantifying the role of atmospheric rivers
764 in the interior western United States. *Atmospheric Science Letters*, 13(4), 257–
765 261. doi: 10.1002/asl.392
- 766 Rutz, J. J., Steenburgh, W. J., & Ralph, F. M. (2014). Climatological charac-
767 teristics of atmospheric rivers and their inland penetration over the west-
768 ern United States. *Monthly Weather Review*, 142(2), 905–921. doi:
769 10.1175/MWR-D-13-00168.1
- 770 Sellars, S. L., Gao, X., & Sorooshian, S. (2015). An object-oriented approach
771 to investigate impacts of climate oscillations on precipitation: A western

- 772 United States case study. *Journal of Hydrometeorology*, 16(2), 830–842.
773 doi: 10.1175/JHM-D-14-0101.1
- 774 Shields, C. A., Rutz, J. J., Leung, L.-Y., Ralph, F. M., Wehner, M., Kawzenuk, B.,
775 ... Nguyen, P. (2018). Atmospheric River Tracking Method Intercomparison
776 Project (ARTMIP): project goals and experimental design. *Geoscientific Model
777 Development*, 11, 2455–2474. doi: 10.5194/gmd-11-2455-2018
- 778 Tung, W.-w., Barthur, A., Bowers, M. C., Song, Y., Gerth, J., & Cleveland, W. S.
779 (2018). Divide and recombine (D&R) data science projects for deep analysis
780 of big data and high computational complexity. *Japanese Journal of Statistics
781 and Data Science*, 1(1), 139–156. doi: 10.1007/s42081-018-0008-4
- 782 Wick, G. A., Neiman, P. J., & Ralph, F. M. (2013). Description and validation
783 of an automated objective technique for identification and characteriza-
784 tion of the integrated water vapor signature of atmospheric rivers. *IEEE
785 Transactions on Geoscience and Remote Sensing*, 51(4), 2166–2176. doi:
786 10.1109/TGRS.2012.2211024
- 787 Wolter, K., & Timlin, M. S. (1993). *Monitoring enso in coads with a seasonally
788 adjusted principal component index.* Paper presented at the 17th Climate
789 Diagnostics Workshop, NOAA/NMC/CAC, NSSL, Oklahoma Clim. Survey,
790 CIMMS and the School of Meteor., Univ. of Oklahoma, Norman, OK.
- 791 Xie, P., Yatagai, A., Chen, M., Hayasaka, T., Fukushima, Y., Liu, C., & Yang, S.
792 (2007). A gauge-based analysis of daily precipitation over East Asia. *J. Hy-
793 drometeorol.*, 8(3), 607–626. doi: 10.1175/JHM583.1
- 794 Zhu, Y., & Newell, R. E. (1998). A proposed algorithm for moisture fluxes from at-
795 mospheric rivers. *Monthly Weather Review*, 126(3), 725–735. doi: 10.1175/
796 1520-0493(1998)126(0725:APAFMF)2.0.CO;2